Mechanical and shape memory properties of NiTi triply periodic minimal surface structures fabricated by laser powder bed fusion

Sun, Lingqi; Chen, Keyu; Geng, Peng; Zhou, Yan; Wen, Shifeng; Shi, Yusheng

DOI
10.1016/j.jmapro.2023.06.034

Publication date
2023

Document Version
Final published version

Published in
Journal of Manufacturing Processes

Journal of Manufacturing Processes 101 (2023) 1091–1100

Contents lists available at ScienceDirect

Journal of Manufacturing Processes

journal homepage: www.elsevier.com/locate/manpro

Mechanical and shape memory properties of NiTi triply periodic minimal surface structures fabricated by laser powder bed fusion

Lingqi Sun [a], Keyu Chen [c], Peng Geng [a,*], Yan Zhou [b], Shifeng Wen [a], Yusheng Shi [a]

[a] State Key Laboratory of Material Processing and Die & Mold Technology, School of Materials Science and Engineering, Huazhong University of Science and Technology, Wuhan, 430074, Hubei, China

[b] National Center of Technology Innovation for Digital Construction, School of Civil and Hydraulic Engineering, Huazhong University of Science and Technology, Wuhan, 430074, Hubei, China

[c] Department of Biomechanical Engineering, Delft University of Technology, Delft, 2628 CD, South Holland, Netherlands

ARTICLE INFO

Keywords:
NiTi alloy
Laser powder bed fusion
Three-period minimum surface
Shape memory effect

ABSTRACT

Porous NiTi lattice structures are widely used in the manufacture of crucial components owing to their excellent shape memory effect, superelasticity, and high damping capacities. However, the specific strength and lightweight characteristics of porous NiTi lattice structures fabricated by conventional technologies are limited by unpredictability. In this work, three types of porous NiTi structures based on triply periodic minimal surface (TPMS) – Diamond, Gyroid, and Primitive – were designed and manufactured by the laser powder bed fusion (LPBF) additive manufacturing process. This work demonstrates LPBF is a feasible and efficient approach to fabricate highly accurate porous NiTi TPMS structures. Moreover, the influence of each of these structures on the mechanical and shape memory properties was investigated. Among the three structures, Gyroid had the smallest volume fraction deviation. Furthermore, the Diamond structure had the largest compressive modulus (782.82 MPa) and ultimate yield strength (163.14 MPa). The Gyroid and Primitive structures exhibit excellent elastic recovery deriving from high values of compressive modulus (662.44 MPa, and 703.29 MPa), and can maintain reliable structural robustness. The Primitive structure exhibited the lowest mechanical properties (37.80 MPa). During the cyclic compression test, Gyroid and Primitive show a smaller unrecovered strain than Diamond. Primitive shows the largest recovered strain during the heating process (6.98%). The higher mechanical flexibility of Primitive structure endows this structure with higher recovery ratio. During the direct compression test, the residual strain exhibits a positive correlation with the loading strain. All three structures exhibit good deformation recovery capability with a strain of 4%. At a strain of 12%, recovered strain during heating became the dominant factor in the recovery of the TPMS structure. Overall, porous NiTi TPMS structures are capable of reversible compressibility composed of rapid elastic recovery and controllable shape memory recovery. The unique performance of porous NiTi TPMS structure fabricated by LPBF renders it a highly efficiency energy-absorbing structure.

1. Introduction

In recent years, reversible energy-absorbing device has been recognized widely as an efficient and safer approach to crash cushioning, soft-landings, energy conversion, etc. [1–4]. Nevertheless, the vital drawbacks of conventional porous structure are the limited capacity for energy absorption and disposable nature [5,6]. The development of high-efficiency and reversible cushioning materials and structures will enable more effective cushioning and safer landings for various applications.

NiTi alloys are used for various applications such as energy absorption, vibration reduction, driving, and structural adaptation [7–9] owing to their excellent shape memory effect, superelasticity and high damping capacities. The shape memory effect (SME) of NiTi alloys enables shape recovery under stress-free conditions, thereby ensuring the cyclic use of the material as an energy-absorbing device [10–12]. The superelasticity enables the generation of giant nonlinear recoverable strains in NiTi alloys upon loading and unloading. In addition,

* Corresponding author.
E-mail addresses: lingqi_sun@hust.edu.cn (L. Sun), K.Chen-6@tudelft.nl (K. Chen), gengpeng@hust.edu.cn (P. Geng), yanzhou@hust.edu.cn (Y. Zhou), roya_wen@hust.edu.cn (S. Wen), yushengshi@hust.edu.cn (Y. Shi).

https://doi.org/10.1016/j.jmapro.2023.06.034
Received 28 February 2023; Received in revised form 17 April 2023; Accepted 15 June 2023
Available online 5 July 2023

the shape memory alloy has the capability to efficiently convert a substantial amount of external mechanical energy into internal energy and dissipate it into the surrounding environment in the form of heat during the deformation process, resulting in an improvement in the energy-absorbing performance. As they offer several advantages, NiTi shape memory alloys are considered promising materials for the manufacture of buffer energy-absorbing devices. Notably, reducing the weight of these materials is crucial to achieving high energy absorption capacities.

Lattice structures have high strength and stiffness and are lightweight. Moreover, they exhibit strong energy absorption and excellent crashworthiness, which is regarded as an essential characteristic of buffer energy-absorbing devices. Lattice structures are porous structures formed by a controlled repetition in the space of a designed base unit cell [13–15]. Among lattice structures, the TPMS structures have been reported to overcome the common defects truss structures, including stress concentration and fragile joints [16,17]. Some common TPMS structures include Schwartz Diamond structure (Diamond), Schoen Gyroid structure (Gyroid) and Schwartz Primitive structure (Primitive). Maskery et al. [18,19] investigated the energy absorption properties of the Gyroid and BCC lattice structures. The results indicated that the Gyroid lattice structure exhibited a threefold increase in energy absorption per unit mass compared to the BCC lattice structure, when subjected to 50% compressive strain. Saghaian et al. [20] investigated the mechanical properties of NiTi TPMS (Primitive, Gyroid, and Diamond) lattice structures fabricated via SLM. By changing the configuration and porosity of the TPMS lattice structure, the elastic modulus of the NiTi alloy sample can be reduced by about 76% to 90%. This indicates that the geometry of the TPMS structure can significantly impact the mechanical properties of the lattice structure. Novak et al. [21] conducted dynamic compression and quasi-static compression experiments on 316L stainless steel cylinders with four different TPMS (Diamond, IWP, Primitive, and Gyroid) lattice structures. The results indicated that the Diamond lattice structure had the highest plateau stress value in both tests, followed by the Gyroid and IWP lattice structures, while the Primitive lattice structure had the lowest plateau stress value.

Additive manufacturing (AM) has received considerable attention over the past few years. Laser powder bed fusion (LPBF) is a widely utilized technique for fabricating metal components with the advantages of high precision and design flexibility. LPBF produces materials digitally *via* layer-by-layer stacking, thereby allowing the formation of dense metal parts. Notably, LPBF is superior to conventional techniques as it enables the fabrication of lightweight porous lattice structures with tunable porosity and mechanical properties, exceeding the capabilities of conventional methods [22]. Salem et al. [23] prepared high-precision and high-density lattice structures. They also elucidated the influence of the parameters on the strut diameter and internal pore morphology of lattice structures. In another study, Han et al. [24] prepared lattice structures with a apparent density of more than 99% by optimizing the SLM process parameters, demonstrating that the technique render good geometric reproducibility, which is essential for fabricating lattice structures.

In this study, three types of TPMS structures – Diamond, Gyroid and Primitive – were prepared by LPBF, and their fabrication accuracy, mechanical properties, fracture behavior and shape memory performance were systematically studied. This work demonstrates the feasibility of utilizing LPBF to fabricate NiTi shape memory material with typical TPMS structure, and the porous NiTi TPMS structure fabricated by LPBF has been substantiated with great potential for energy-absorbing.

2. Material and experimental

2.1. Design of TPMS lattice structures

The implicit function of TPMS lattice structures is designed and modeled by MATLAB software. The mathematical functions of the TPMS-based Gyroid surface, TPMS-based Diamond surface and TPMS-based Primitive surface can be expressed in the following Eqs. (1), (2) and (3), respectively:

Diamond structure:

$$\sin X \sin Y \sin Z + \sin X \cos Y \cos Z + \cos X \sin Y \cos Z + \cos X \cos Y \sin Z = t \quad (1)$$

Gyroid structure:

$$\sin X \cos Y + \sin Y \cos Z + \sin Z \cos X = t \quad (2)$$

Primitive structure:

$$\cos X + \cos Y + \cos Z = t \quad (3)$$

in which, $X = 2\alpha\pi x$, $Y = 2\beta\pi y$, $Z = 2\gamma\pi z$, α, β and γ are constants related to the unit cell size in the x, y, and z directions, respectively. Parameter t controls the volume surrounded by the structure.

Since the surface generated by mathematical functions has no thickness, it needs to be thickened into a solid structure when it is used in LPBF process. There are two common methods to create TPMS lattice materials based on zero-thickness surface. The first method is to make a solid domain between the minimum surface and volume, and to create a solid lattice for the part $\phi(x, y, z) \leq t$ or $\phi(x, y, z) \geq t$. The second is to offset the minimum surface along its normal direction, that is, to form two surfaces by -C ≤ (x, y, z) ≥ C, and create solid lattices from the space between the two surfaces. The second method was adopted in this paper. This paper focused on the effect of different TPMS structures on mechanical and shape memory properties. Hence, three structures were constructed with the same number of crystal cells (5 × 5 × 4), the same total size (31 mm × 31 mm × 25 mm) and the same volume fraction (12.5%).

2.2. Material and fabrication

Raw NiTi powder material was prepared by the gas atomization method (Shenzhen Minatech Co., Ltd., China). Morphology and particle size distribution of the powder (Fig. 1) were measured using a field-electron scanning electron microscope (Quanta 450, FEI, US) and a laser particle size analyzer (Mastersizer 3000, Malvern Panalytical, England). The powder exhibited a spherical or near-spherical morphology (Fig. 1a). The particle size was determined to be in the range of ranged from 24.5 to 63.8 μm (Fig. 1b).

NiTi TPMS samples were prepared using a commercial SLM 125 metal 3D printer (SLM Solution, Germany) under a highly pure argon atmosphere. First, an NiTi substrate was preheated to 200 °C, and then argon gas was pumped into the molding chamber to maintain an oxygen concentration below than 200 ppm. The process parameters were optimized and set as follows: laser power (P) of 250 W, laser scanning speed (v) of 1000 mm/s, powder layer thickness (t) of 0.03 mm and scanning distance (h) of 0.12 mm; laser energy density [$E = P/vht$] was calculated to be 69.40 J/mm^3.

2.3. Measurement and characterization

The density of solid pillars was measured using the Archimedes drainage method. The density of all samples was calculated over 97% for all samples.

The TPMS lattice structures were scanned and reconstructed using a microfocus X-ray computed tomography (micro-CT) (Cheetah EVO, Comet Yxlon GmbH, Germany), and the micro-CT reconstructed models were aligned with the original CAD using VG Studio MAX2.2 software. A comparison between the model and the actual lattice was conducted to analyze surface deviation.

Uniaxial compression tests were performed using a universal testing machine (SHT4206, Sansi Yongheng Co., Ltd., China). The dimensions of the test sample are 31 ± 0.42 mm × 31 ± 0.35 mm × 25 ± 0.47 mm.

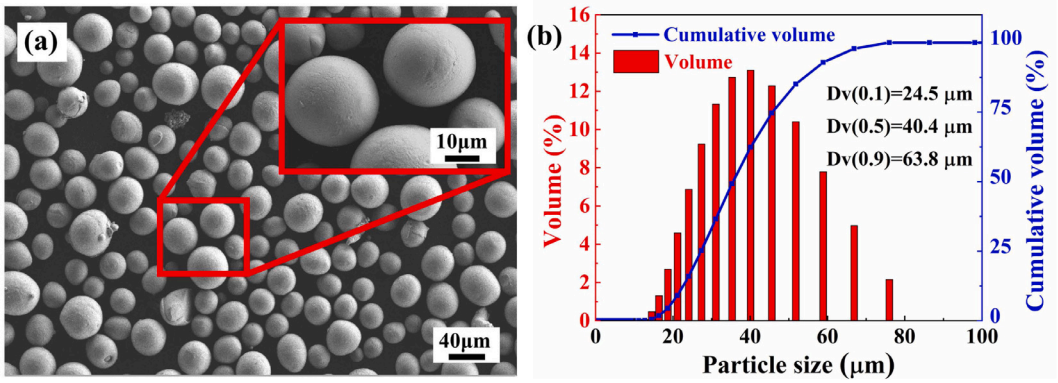

Fig. 1. (a) Morphology and (b) particle size distribution of the NiTi powder.

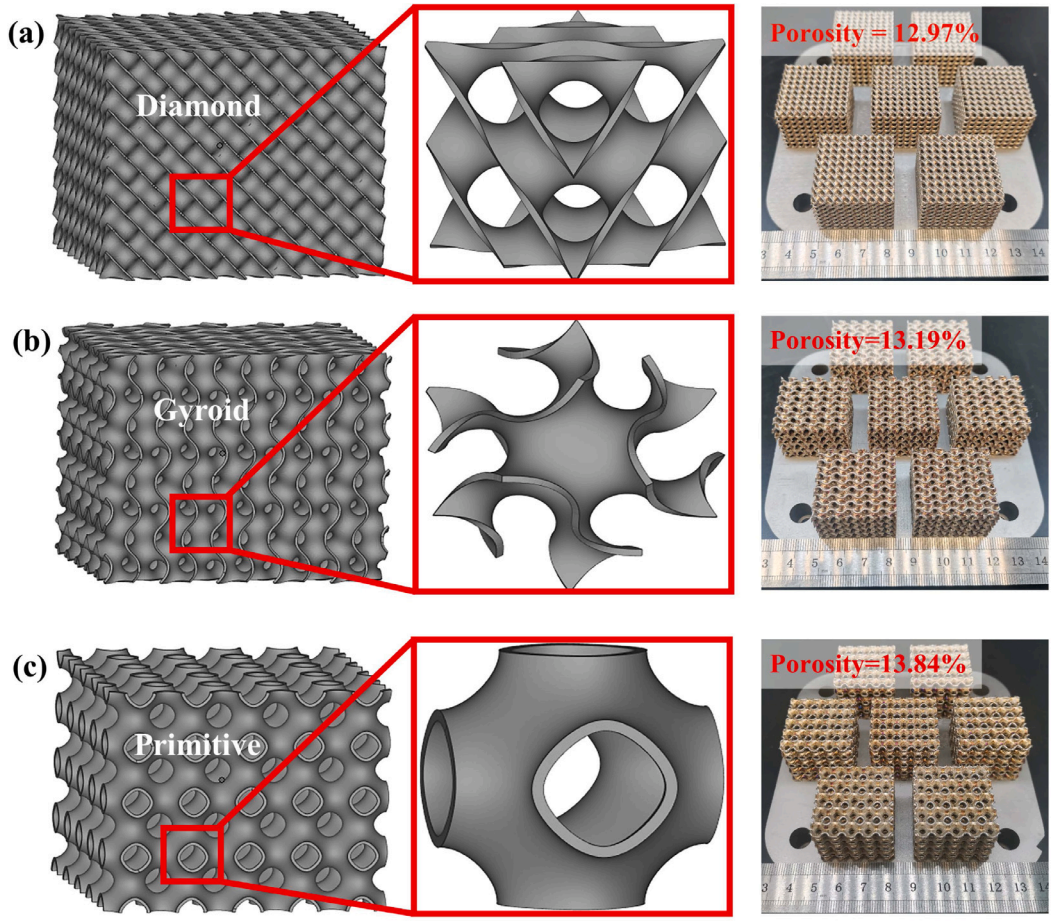

Fig. 2. STL model, unit cell models, and photographs of prepared samples: (a) Diamond structure, (b) Gyroid structure, and (c) Primitive structure.

Compression tests were carried out according to ISO 4506-2018 standard. The loading rate was 1.5 mm/min. Compressive stress–strain curves are used to determine the compressive modulus, nominal yield strength and ultimate strength. The stress at which the curve deviates from 0.2% strain in the elastic–plastic deformation region is defined as nominal yield strength. Each value of a mechanical property is the average value of three samples.

In order to investigate the shape memory behavior of the NiTi TPMS structure, the samples underwent compression testing under various loading conditions. During the cyclic compression test, the samples were subjected to loading–unloading experiments with a 2% strain increment at room temperature. The experiment was terminated when the compressive strain value reached 12%. During the direct compression test, the samples were compressed with a strain of 4%, 8%, and 12% at room temperature. Following unloading, the compressed samples were immersed in a silicone oil bath at 150 °C to enable shape recovery. In a typical procedure, the sample was firstly compressed and reached the strain ϵ_{load} under load. The stress was subsequently removed, the ratio of the rebound size of the sample to the original height is referred to as the elastic strain (ϵ_{ela}). Under a stress-free condition, recovery is accomplished by heat the sample to a recovery temperature, leading to a SME recovered strain ϵ_{rec}. The remaining strain after all processes is referred to as residual strain ϵ_{res}.

The characteristic temperature of the martensitic transformation was measured *via* differential scanning calorimetry (DSC) (Q2000, TA, US). The sample began to heat from 193 K to 393 K, and then

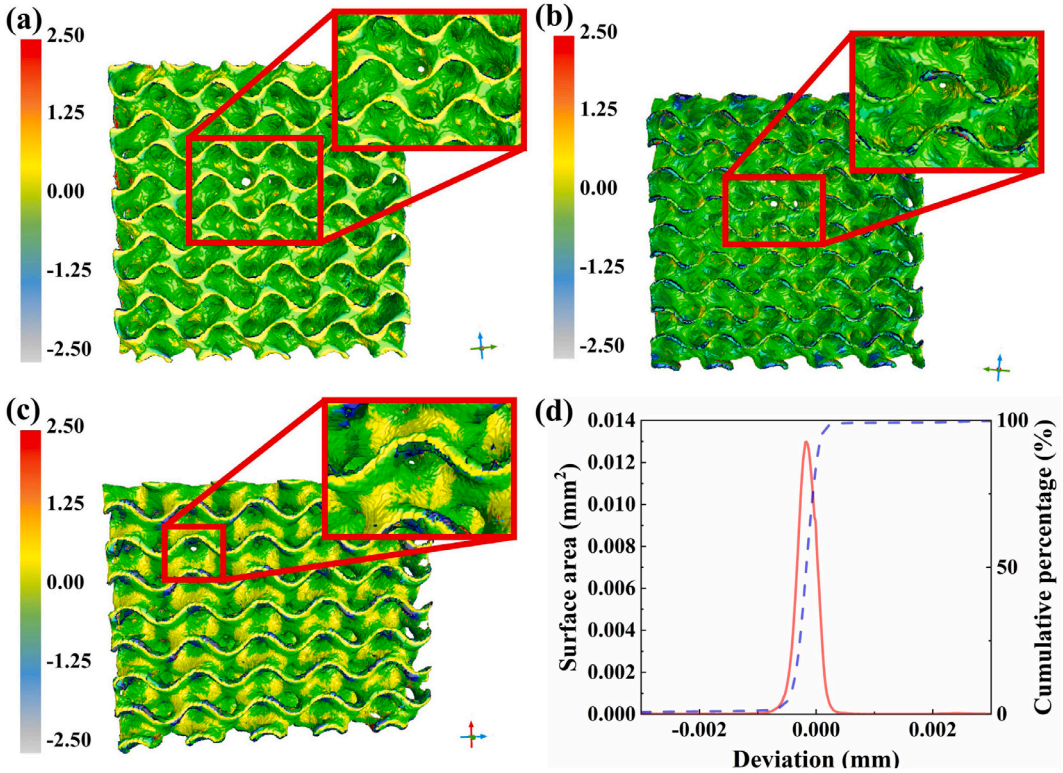

Fig. 3. Deviation plots for (a) Bottom; (b) top; (c) side surface; and (d) statistical surface deviation distribution curve.

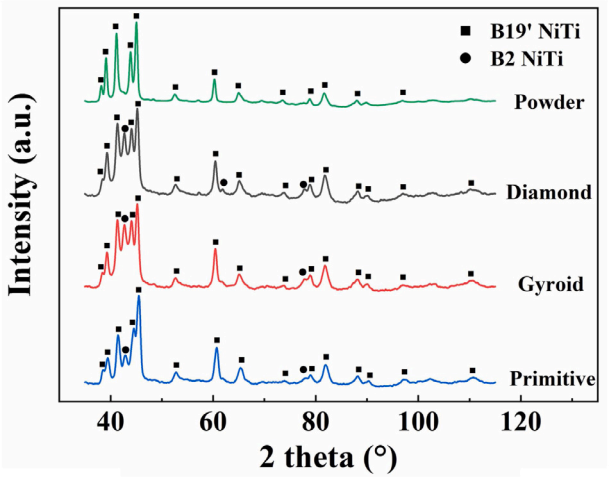

Fig. 4. XRD patterns of NiTi powder and three NiTi TPMS structures.

cooled to 193 K, with the rate of 10 K/min. The start, peak and end temperatures of the forward martensitic transformation (Ms, Mp and Mf), and the start, peak and end temperatures of the inverse martensitic transformation (As, Ap and Af) were obtained from the DCS curves.

The phase composition of the porous TPMS lattice structure was measured *via* X-ray diffraction (XRD-7000, Shimadzu, Japan) in the 2θ range from 35° to 115° at a scanning rate of 10 °/min.

3. Results and discussion

3.1. Sample morphology and phase identification

Fig. 2 shows the theoretical models, unit cell models and photographs of samples fabricated by LPBF, corresponding to three types of TPMS structures [(a) Diamond, (b) Gyroid, and (c) Primitive]. The optical morphology data for the samples indicated that, there were no broken rods or units, demonstrating good formability. A comparison of the top and side views of all samples showed that more unmelted powder particles were stuck to the lower surfaces of the samples than to their upper surfaces. Adhesion of the particles could be mainly attributed to thermal diffusion from the molten pool to the surrounding loose powder, which is an inherent limitation of the LPBF process and is unavoidable [25–27].

The LPBF process involves spreading powders layer by layer and then fusing them selectively using a laser. A unique heat-affected zone forms around the molten pool because of thermal diffusion, and the metal powder around the molten pool partially melts and adheres to the solidified rods in a sintered state. The spheroidization and agglomeration of the partially molten powder further aggravated the powder adhesion. Adhesion of powder significantly reduces the surface quality of products fabricated by LPBF.

Fig. 3 shows the surface deviation and statistical surface deviation distribution plots obtained by overlapping the micro-CT reconstruction model of the NiTi Gyroid lattice structure with the designed STL model Fig. 3a and b are the profile comparison of the vertical section and the diagonal section, respectively. As observed, contour lines for the micro-CT reconstruction model deviate from those for the design model. This deviation could be attributed adhesion of unmelted powder particles. A statistical surface deviation distribution curve showing Gaussian distribution is given in Fig. 3c. The relatively small range, from −0.0008 mm to 0.0004 mm, indicates that the NiTi TPMS lattice structure of NiTi TPMS prepared by LPBF has good fabrication accuracy. As observed in Fig. 3d–f, side surface has a larger deviation than the top and bottom surface, which is consistent with the shown in Fig. 2.

Fig. 4 shows the XRD patterns of the prepared samples (three types of TPMS structures) and the starting NiTi powder. As observed, the samples comprise two phases: austenite (B2) and martensite (B19').

Fig. 5 shows the DSC curves of the prepared TPMS samples and the starting NiTi powder. The B2–B19' transition temperatures are listed in

Table 1
Phase transformation data for NiTi TPMS structures prepared by LPBF.

Samples	Heating			Cooling		
	As (°C)	Ap (°C)	Af (°C)	Ms (°C)	Mp (°C)	Mf (°C)
Powder	53.0 ± 1.1	60.1 ± 0.4	90.6 ± 0.3	43.5 ± 2.1	32.4 ± 0.5	20.6 ± 3.6
Diamond	120.0 ± 3.5	128.4 ± 0.8	146.6 ± 2.7	70.9 ± 2.3	46.1 ± 0.6	15.8 ± 2.9
Gyroid	117.0 ± 2.8	128.4 ± 1.1	151.7 ± 2.5	70.1 ± 3.5	43.1 ± 0.9	12.9 ± 2.4
Primitive	109.2 ± 2.1	126.0 ± 0.6	135.9 ± 1.5	69.7 ± 2.6	56.5 ± 1.3	27.1 ± 1.2

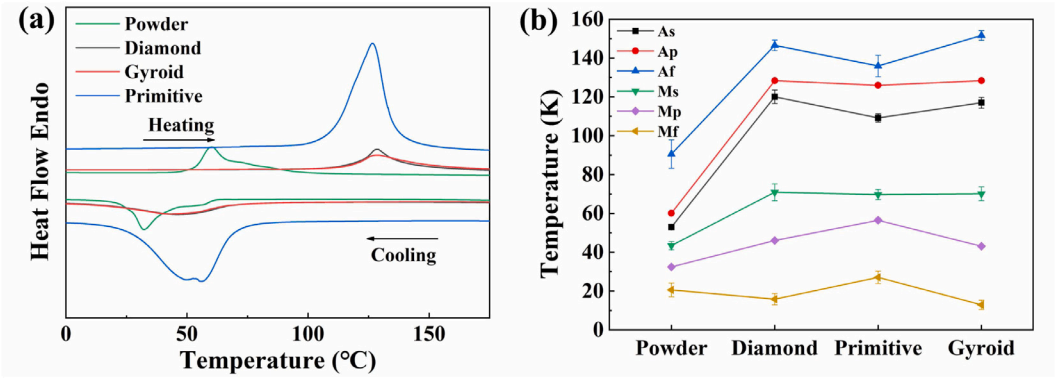

Fig. 5. (a) DSC curves of prepared samples and starting NiTi powder; and (b) phase transition data for martensite and austenite.

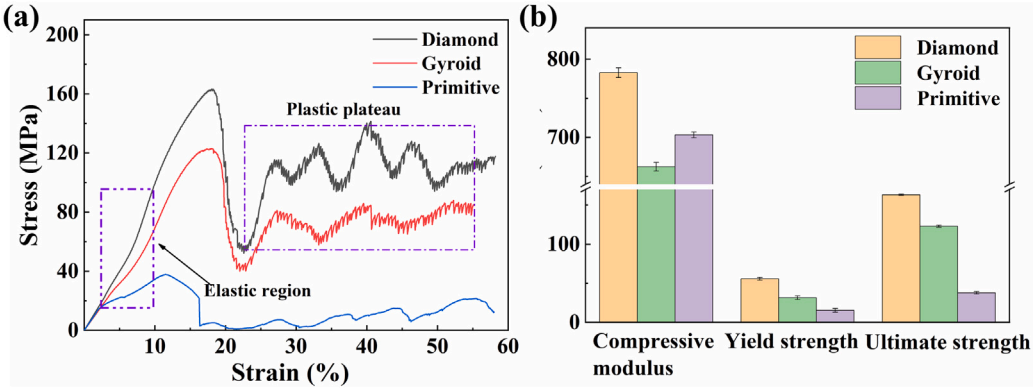

Fig. 6. (a) Compressive stress–strain curves of Diamond, Gyroid and Primitive structures; and (b) corresponding compressive modulus, yield strength, and ultimate yield strength data.

Table 1. As observed, the As, Ap, Af, Ms, and Mp of the starting NiTi powder are higher than those of the TPMS samples. However, Mf of the starting powder is in between that of the samples. Moreover, among the three structures, Primitive shows the highest Mp and Mf, but the lowest Af and As. Nevertheless, all structures show similar Ap and Ms.

3.2. Mechanical properties

Fig. 6a is the uniaxial compressive stress–strain curves for Diamond, Gyroid and Primitive lattice structures. The first stage of each curve, where stress increases linearly with strain, corresponds to elastic deformation; the slope represents the compressive modulus. The second stage corresponds to elastic–plastic deformation. In this stage, stress increases nonlinearly with strain before reaching the maximum value. Subsequently, a considerable dip appears in the stress–strain curve. The stress at which the curve deviates from 0.2% strain in the elastic–plastic deformation region is defined as yield strength. The third stage corresponds to failure of the structure units. Fluctuations in the stress–strain curves of the structures indicate fracture and collapse of rods under the critical stress condition. Finally, the stress–strain curve will continue showing a positive hardening slope indicating fracture of all layers.

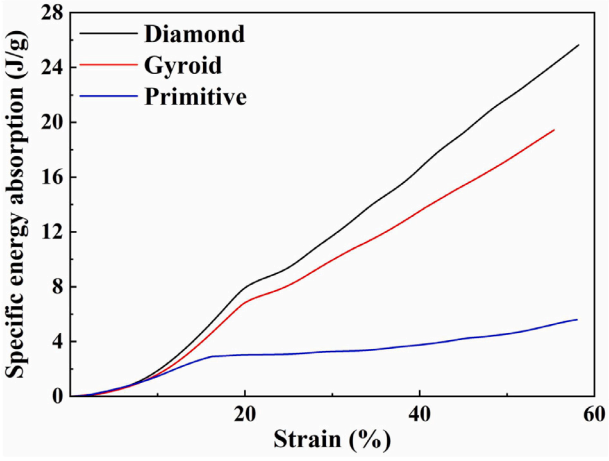

Fig. 7. Energy absorption diagram of TPMS.

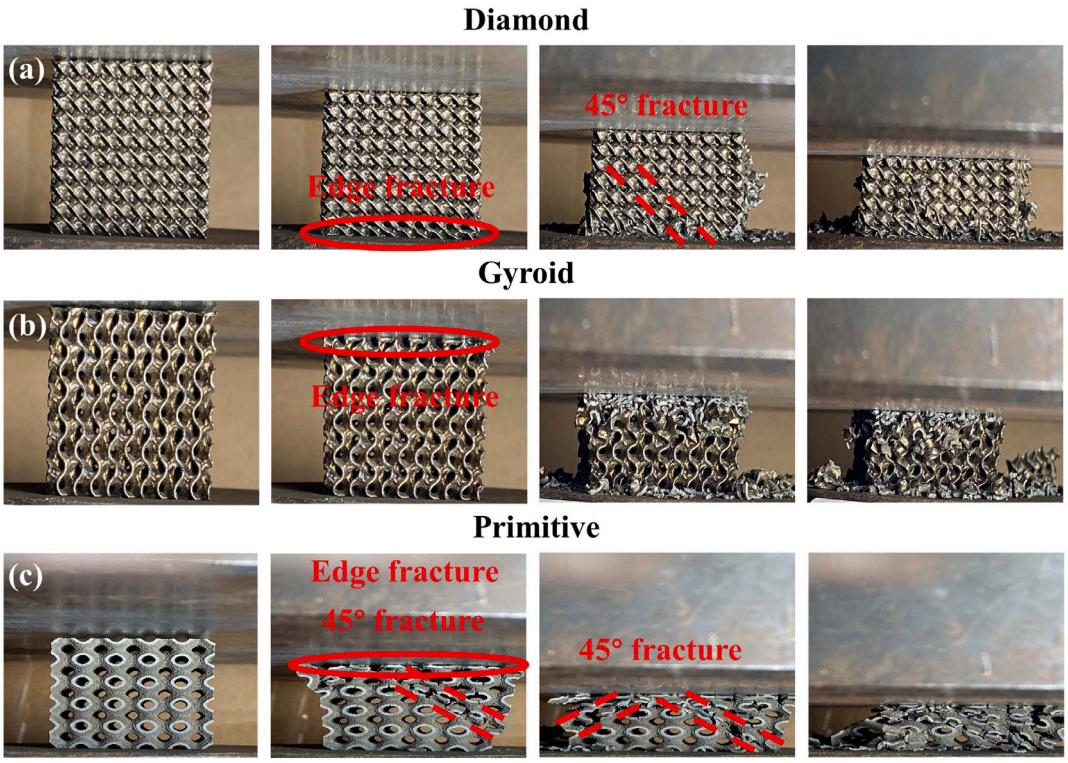

Fig. 8. Images captured during uniaxial compression analysis tests at different strain levels for (a) Diamond, (b) Gyroid, and (c) Primitive TPMS structures.

Yang et al. [28] studied the mechanical behavior of a 316L stainless steel TPMS structure. The compressive modulus of the sample was measured to be 1097.87 ± 20.85 MPa, while the ultimate yield strength was found to be 19.15 ± 0.45 MPa. Sun et al. [29] studied the mechanical properties of Ti6Al4V Diamond, Gyroid, and Primitive TPMS structures, reporting Young's modulus values of 2238 MPa, 1641 MPa and 614 Mpa, ultimate yield strengths of 102.4 MPa, 61.8 MPa and 23.5 MPa, and specific energy absorption values of 0.048 J/g, 0.038 J/g and 0.017 J/g, respectively. The LPBFed NiTi TPMS structure has a lower strength compared to the Ti6Al4V TPMS structure, but its modulus is similar, and it has a better specific energy absorption values. Ge et al. [30] found that the compression behavior of Ti6Al4V TPMS samples was brittle fracture, and the compressive modulus of Gyroid (5.58 GPa) with wall thickness was similar to the current experiment, while the ultimate yield strength (34.62 MPa) was much smaller. The lower compressive modulus indicates a better cushioning effect, while the higher ultimate yield strength suggests better mechanical properties and energy absorption capacity. The stress–strain curve comprised a plateau-like region (i.e., the hardening slope was approximated as zero). This plateau-like region and hardening slope behavior were attributed to different mechanisms, depending on the material properties. Notably, the governing mechanisms for elastomeric and brittle materials have been determined to be buckling and fracturing, respectively. Nonetheless, for ductile materials, the controlling mechanism was determined to be plastic yielding [31]. When NiTi alloy was subjected to compressive deformation, the stress–strain curve did not show a stress plateau owing to continuous work hardening of the material [32–34]. On the basis of these reports, we could infer that in this study, the mechanical properties of NiTi TPMS samples were influenced by both material properties and structural architecture.

According to the stress–strain curves, the samples underwent elastic deformation before reaching the initial ultimate stress, and then collapsed, losing most of the strength. This sudden collapse represented the characteristic failure behavior of brittle porous materials at low degrees of deformation. After first collapsing, the remaining structure was found to regain strength. The samples exhibited a cascading collapse throughout the subsequent process and showed an upward trend.

Fig. 6b shows the compressive modulus, yield strength and ultimate yield strength data for the three TPMS lattice structures prepared in this study. As observed, the yield strengths of Diamond (55.73 MPa), Gyroid (31.58 MPa) and Primitive (15.37 MPa) are similar. The compression modulus of Diamond, Gyroid and Primitive are 782.82 MPa, 662.44 MPa, and 703.29 MPa, respectively, and the ultimate yield strength are 163.14 MPa, 122.90 MPa 37.80 MPa, respectively. As indicated in Fig. 6b, Diamond possesses optimal compressive properties, while Primitive possesses the least attractive compressive properties among the three structures.

Fig. 7 shows the absorbed energy per unit mass of the prepared samples. As observed, each energy curve rises gradually at the beginning corresponding to the first stage of the stress–strain curves of the TMPS structures. Subsequently, the curves experience a precipitous decline in slope as the structures undergo their initial collapse. Moreover, the Diamond and Gyroid structure exhibit superior energy absorption capabilities compared to the Primitive structure, particularly when stress–strain the curves exhibit yield plateaus.

Optical images of Diamond, Gyroid, and Primitive recorded during uniaxial compression analysis are given in Fig. 8. The images illustrate deformation evolution of the structures. In each structure, the initial fractures appear at the edges of the structures, which are a part of the fragmented unit cells of the whole structure. Moreover, fractures form at an angle of 45° within the structure.

SEM images of the three lattice structures subject to uniaxial compression are given in Fig. 9. The images show fractures formed in the structures. As observed, the NiTi TPMS structures exhibit cleavage fractures without any significant macroscopic plastic deformation near the fractures. The crack propagation area is a flat dimple, which is typical brittle fracture characteristics. This indicates that the fracture mode of the NiTi TPMS lattice structure fabricated by LPBF undergo brittle failure.

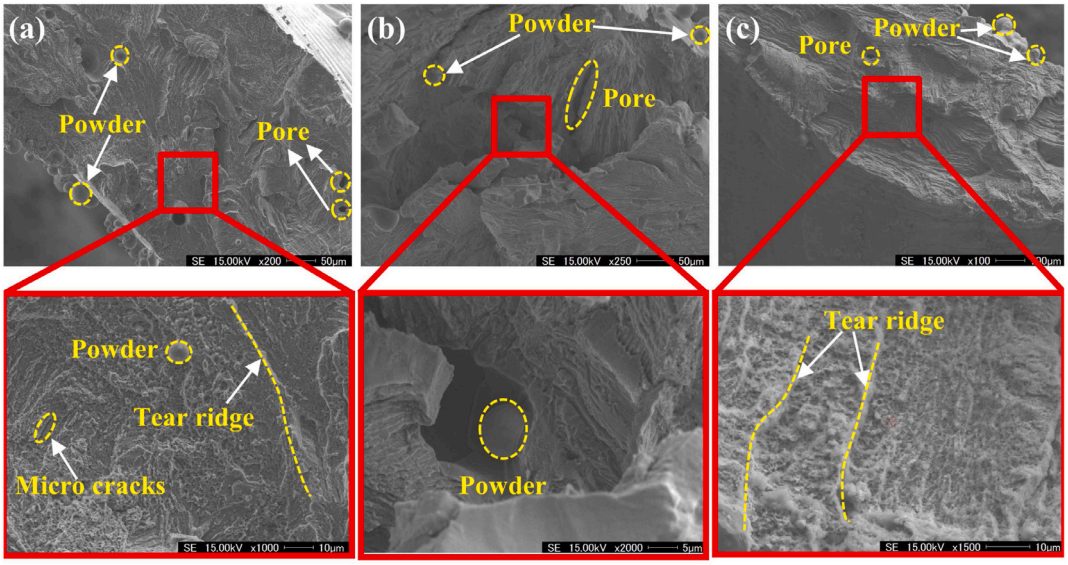

Fig. 9. SEM image of fracture surfaces. (a) Diamond structure, (b) Gyroid structure, and (c) Primitive structure.

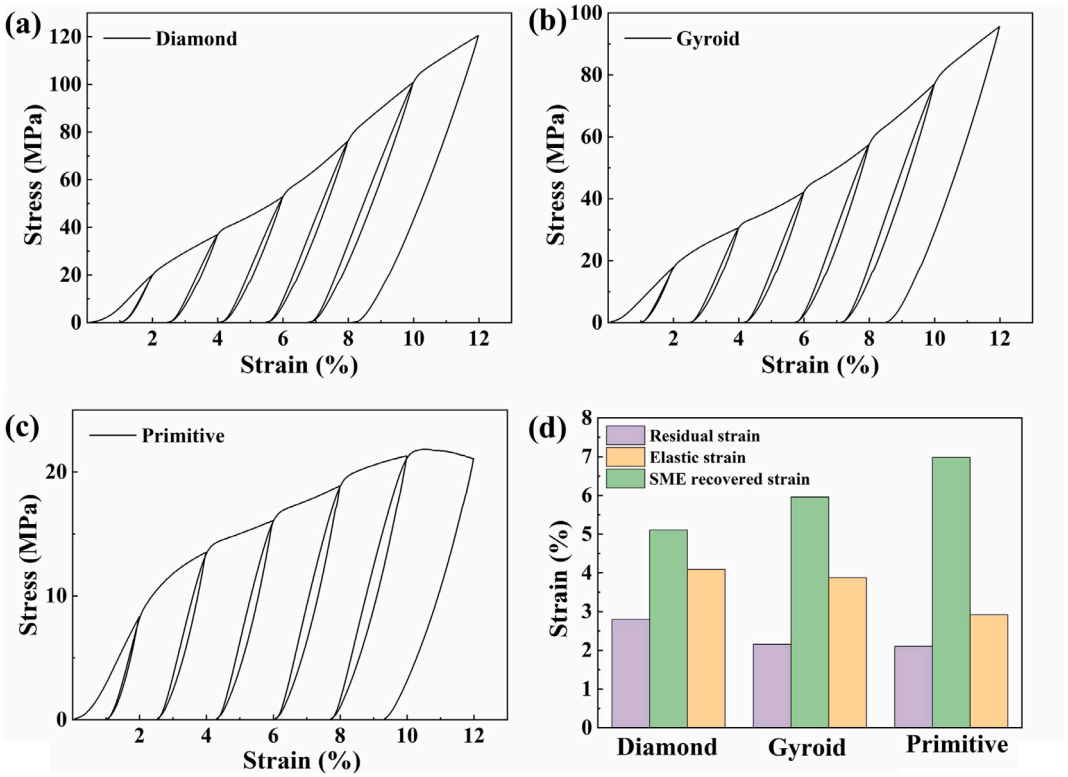

Fig. 10. (a–c) Cyclic compression curves; and (d) elastic strain, SME recovered strain and residual strain of Diamond, Gyroid, and Primitive TPMS structures.

3.3. Shape memory performance

Fig. 10a–c show the stress–strain curves of the three lattice structures subject to a cyclic compression test. Fig. 10d shows elastic strain ϵ_{ela}, SME recovered strain ϵ_{rec} and residual strain ϵ_{res} of the structures. As observed, Gyroid and Primitive show a smaller unrecovered strain than Diamond. Moreover, Primitive shows the largest recovered strain during the heating process. Yang et al. [35] reported that the total shape recovery ratio of NiTi Gyroid TPMS was 96.5% with a strain of 8%. According to Zhang et al. [36], after 15 compression cycles of the NiTi Gyroid TPMS, the residual strain increased from 2.8% to 4%. The residual strain is mainly caused by functional fatigue behavior under cyclic loading condition.

Fig. 11a–c show elastic strain ϵ_{ela}, SME recovered strain ϵ_{rec} and residual strain ϵ_{res} of the three NiTi TPMS structures measured during the direct compression test. Fig. 11d–f show ϵ_{ela}, ϵ_{rec} and ϵ_{res} of the three NiTi TPMS structures at different strain levels. As observed, residual strain increases with an increase in compressive strain. Moreover, SME recovered strain of Diamond and Gyroid structures increases with the strain, while that of the Primitive structure first increases and then decreases.

When compressed with a strain of 4%, all TPMS structures exhibit a superior recovery strain (ϵ_{ela} and ϵ_{rec}). Under high strain levels,

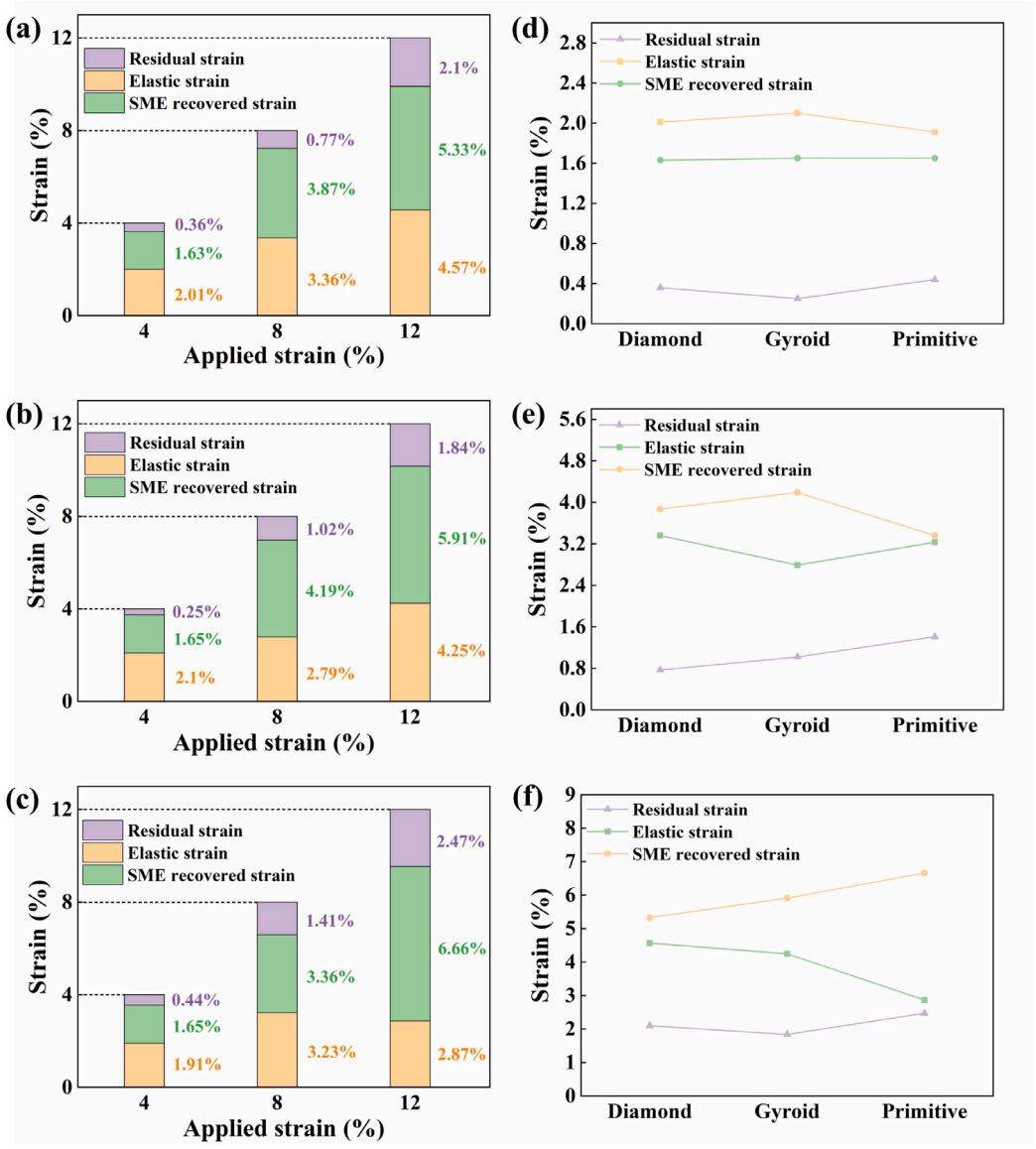

Fig. 11. Elastic strain, SME recovered strain and residual strain of (a) Diamond, (b) Gyroid, and (c) Primitive TPMS structures.

the Primitive structure firstly exhibits fracture and collapse of rods. Notably, when the strain level reaches 12%, the fracture of rods results in a notable reduction of elastic strain. This phenomenon is caused by the presence of excessive stress during compression, which leads to collapse of rods, and finally, irreversible deformation of the structure. As observed from the DSC curves in Fig. 5, Mf of the three TPMS lattice structures is close to room temperature, while Ms is higher than RT. This indicates that austenite is the dominant phase in all the three lattice structures, and that compressive deformation recovery of the structures at room temperature is mainly induced by stress. Recovery deformation after unloading mainly corresponds to the superelastic response, wherein a part of the stress-induced martensite spontaneously re-transforms into austenite, induced by free energy and elastic strain energy. Recovery deformation after heating is mainly caused by partial stress-induced martensite retention at room temperature. When the deformed material is heated above Af, martensite formed due to residual stress re-transforms into austenite, leading to residual recovery deformation. Non-recovery deformation is mainly caused by the permanent collapse of the internal TPMS structure under high stress.

4. Conclusions

In this study, three types of NiTi TPMS structures – Diamond, Gyroid and Primitive – were fabricated by LPBF and the samples were analyzed systematically. The main conclusions are given below. The NiTi TPMS structures fabricated by LPBF showed high fabrication accuracy. Moreover, thermal analysis of the samples revealed that the structures possessed high crystallinity and thermodynamic stability. Uniaxial compression analysis showed that the ultimate yield strengths of the structures decreased in the following order: Diamond > Gyroid > Primitive. Although ultimate yield strengths of the structures were considerably different, their compressive moduli were similar. This is due to a combination of material properties and structural architecture; the compression modulus is mainly influenced by the material characteristics of NiTi; the comparatively high ultimate yield strength of Diamond could be attributed to the presence of less stress.

Notably, the NiTi TPMS samples exhibited excellent shape memory performance. Among all the three structures, Primitive showed the smallest residual strain and the largest SME recovered strain. Moreover, recovery deformation of the Diamond and Gyroid structures increased

with compressive strain, while that of the Primitive structure first increased and then decreased. This was mainly attributed to excessive stress during compression, which led to failure of the rods, and finally, irreversible deformation. The mechanical properties of each structure varied as a function of loading conditions because NiTi alloy undergoes continuous work hardening when subject to compression deformation. In addition, the properties were significantly influenced by the deformation process.

Our study demonstrates that LPBFed NiTi TPMS structures not only exhibit high accuracy but also exceptional energy absorption capabilities. NiTi TPMS structures are a potential candidate for various engineering applications, including crash cushioning, soft-landings, vibration isolators, etc. For example, the soft-landing of probes requires a buffer landing mechanism, which commonly uses aluminum alloy honeycomb structure. However, its one-time use and limited buffer energy absorption efficiency are significant drawbacks. LPBFed NiTi TPMS structures retain the unique properties of NiTi alloy and improve cushioning properties via structural optimization. NiTi alloys' shape memory effect allows for cyclic use of buffer landing mechanisms. The TPMS structure endows the device's high energy absorption and vibration reduction capabilities. Thus, LPBFed NiTi TPMS structures can be directly used as functional components in the actual engineering domain.

CRediT authorship contribution statement

Lingqi Sun: Investigation, Writing – original draft. **Keyu Chen:** Writing – review & editing. **Peng Geng:** Formal analysis, Conceptualization. **Yan Zhou:** Funding acquisition. **Shifeng Wen:** Conceptualization. **Yusheng Shi:** Supervision.

Declaration of competing interest

The authors declare that they have no known competing financial interests or personal relationships that could have appeared to influence the work reported in this paper.

Acknowledgments

This work was funded by the National Natural Science Foundation of China (No. 52275332), Key Research & Development Program of Hubei Province, China (No. 2020BAB045), State Key Laboratory of Materials Processing and Die & Mould Technology, Huazhong University of Science and Technology, China (No. P2022-001) and the Sixth China Association of Science and Technology Youth Talents Invitation Project, China (No. YESS20200326).

References

[1] Ha NS, Lu G. A review of recent research on bio-inspired structures and materials for energy absorption applications. Composites B 2020;181:107496. http://dx.doi.org/10.1016/j.compositesb.2019.107496.

[2] Xu F, Zhang X, Zhang H. A review on functionally graded structures and materials for energy absorption. Eng Struct 2018;171:309–25. http://dx.doi.org/10.1016/j.engstruct.2018.05.094.

[3] Baroutaji A, Sajjia M, Olabi A-G. On the crashworthiness performance of thin-walled energy absorbers: Recent advances and future developments. Thin Wall Struct 2017;118:137–63. http://dx.doi.org/10.1016/j.tws.2017.05.018.

[4] Bodaghi M, Serjouei A, Zolfagharian A, Fotouhi M, Rahman H, Durand D. Reversible energy absorbing meta-sandwiches by FDM 4D printing. Int J Mech Sci 2020;173:105451. http://dx.doi.org/10.1016/j.ijmecsci.2020.105451.

[5] Tsang H, Raza S. Impact energy absorption of bio-inspired tubular sections with structural hierarchy. Compos Struct 2018;195:199–210. http://dx.doi.org/10.1016/j.compstruct.2018.04.057.

[6] Abdullah N, Sani M, Salwani M, Husain N. A review on crashworthiness studies of crash box structure. Thin Wall Struct 2020;153:106795. http://dx.doi.org/10.1016/j.tws.2020.106795.

[7] Sam J, Franco B, Ma J, Karaman I, Elwany A, Mabe J. Tensile actuation response of additively manufactured nickel-titanium shape memory alloys. Scr Mater 2018;146:164–8. http://dx.doi.org/10.1016/j.scriptamat.2017.11.013.

[8] Zou P, Zheng C, Hu L, Wang H. Rapid growth of TiNi intermetallic compound within undercooled Ti50Ni50 alloy under electrostatic levitation condition. J Mater Sci Technol 2021;77:82–9. http://dx.doi.org/10.1016/j.jmst.2020.10.064.

[9] Mahtabi MJ, Stone TW, Shamsaei N. Load sequence effects and variable amplitude fatigue of superelastic NiTi. Int J Mech Sci 2018;148:307–15. http://dx.doi.org/10.1016/j.ijmecsci.2018.08.037.

[10] Zhang D, Hu Z, Li Y, Cong W. Excellent damping properties and their correlations with the microstructures in the NiTi alloys fabricated by laser-directed energy deposition. J Manuf Process 2022;84:965–76. http://dx.doi.org/10.1016/j.jmapro.2022.10.047.

[11] Heller L, Šittner P, Sedlák P, Seiner H, Tyc O, Kadeřávek L, Sedmák P, Vronka M. Beyond the strain recoverability of martensitic transformation in niti. Int J Plasticity 2019;116:232–64. http://dx.doi.org/10.1016/j.ijplas.2019.01.007.

[12] Ossmer H, Chluba C, Kauffmann-Weiss S, Quandt E, Kohl M. TiNi-based films for elastocaloric microcooling— Fatigue life and device performance. APL Mater 2016;4(6):064102. http://dx.doi.org/10.1063/1.4948271.

[13] Korkmaz ME, Gupta MK, Robak G, Moj K, Krolczyk GM, glu MK. Development of lattice structure with selective laser melting process: A state of the art on properties, future trends and challenges. J Manuf Process 2022;81:1040–63. http://dx.doi.org/10.1016/j.jmapro.2022.07.051.

[14] Maconachie T, Leary M, Lozanovski B, Zhang X, Qian M, Faruque O, Brandt M. SLM lattice structures: Properties, performance, applications and challenges. Mater Des 2019;183:108137. http://dx.doi.org/10.1016/j.matdes.2019.108137.

[15] Al-Saedi DS, Masood S, Faizan-Ur-Rab M, Alomarah A, Ponnusamy P. Mechanical properties and energy absorption capability of functionally graded F2BCC lattice fabricated by SLM. Mater Des 2018;144:32–44. http://dx.doi.org/10.1016/j.matdes.2018.01.059.

[16] Zhang L, Feih S, Daynes S, Chang S, Wang MY, Wei J, Lu WF. Energy absorption characteristics of metallic triply periodic minimal surface sheet structures under compressive loading. Addit Manuf 2018;23:505–15. http://dx.doi.org/10.1016/j.addma.2018.08.007.

[17] Al-Ketan O, Abu Al-Rub RK. Multifunctional mechanical metamaterials based on triply periodic minimal surface lattices. Adv Eng Mater 2019;21(10):1900524. http://dx.doi.org/10.1002/adem.201900524.

[18] Maskery I, Aboulkhair N, Aremu A, Tuck C, Ashcroft I, Wildman R, Hague R. A mechanical property evaluation of graded density Al-Si10-Mg lattice structures manufactured by selective laser melting. Math Sci Eng A-Struct 2016;670:264–74. http://dx.doi.org/10.1016/j.msea.2016.06.013.

[19] Maskery I, Aboulkhair N, Aremu A, Tuck C, Ashcroft I. Compressive failure modes and energy absorption in additively manufactured double gyroid lattices. Addit Manuf 2017;16:24–9. http://dx.doi.org/10.1016/j.addma.2017.04.003.

[20] Saghaian S, Amerinatanzi A, Moghaddam N, Majumdar A, Nematollahi M, Saedi S, Elahinia M, Karaca H. Mechanical and shape memory properties of triply periodic minimal surface (TPMS) NiTi structures fabricated by selective laser melting. Biol. Biol Eng Med 2018;3:1–7. http://dx.doi.org/10.15761/BEM.1000152.

[21] Novak N, Al-Ketan O, Krstulović-Opara L, Rowshan R, Abu Al-Rub RK, Vesenjak M, Ren Z. Quasi-static and dynamic compressive behaviour of sheet TPMS cellular structures. Compos Struct 2021;266:113801. http://dx.doi.org/10.1016/j.compstruct.2021.113801.

[22] Liu J, Guo K, Sun J, Sun Q, Wang L, Li H. Compressive behavior and vibration-damping properties of porous ti-6al-4V alloy manufactured by laser powder bed fusion. J Manuf Process 2021;66:1–10. http://dx.doi.org/10.1016/j.jmapro.2021.03.060.

[23] Salem H, Carter L, Attallah M, Salem H. Influence of processing parameters on internal porosity and types of defects formed in Ti6Al4V lattice structure fabricated by selective laser melting. Math Sci Eng A-Struct 2019;767:138387. http://dx.doi.org/10.1016/j.msea.2019.138387.

[24] Han C, Li Y, Wang Q, Wen S, Wei Q, Yan C, Hao L, Liu J, Shi Y. Continuous functionally graded porous titanium scaffolds manufactured by selective laser melting for bone implants. J Mech Behav Biomed 2018;80:119–27. http://dx.doi.org/10.1016/j.jmbbm.2018.01.013.

[25] Gu D, Shi X, Poprawe R, Bourell DL, Setchi R, Zhu J. Material-structure-performance integrated laser-metal additive manufacturing. Science 2021;372(6545):eabg1487. http://dx.doi.org/10.1126/science.abg1487.

[26] Singla AK, Banerjee M, Sharma A, Singh J, Bansal A, Gupta MK, Khanna N, Shahi A, Goyal DK. Selective laser melting of Ti6Al4V alloy: Process parameters, defects and post-treatments. J Manuf Process 2021;64:161–87. http://dx.doi.org/10.1016/j.jmapro.2021.01.009.

[27] Cooke S, Ahmadi K, Willerth S, Herring R. Metal additive manufacturing: Technology, metallurgy and modelling. J Manuf Process 2020;57:978–1003. http://dx.doi.org/10.1016/j.jmapro.2020.07.025.

[28] Yang L, Yan C, Cao W, Liu Z, Song B, Wen S, Zhang C, Shi Y, Yang S. Compression–compression fatigue behaviour of gyroid-type triply periodic minimal surface porous structures fabricated by selective laser melting. Acta Mater 2019;181:49–66. http://dx.doi.org/10.1016/j.actamat.2019.09.042.

[29] Sun Q, Sun J, Guo K, Wang L. Compressive mechanical properties and energy absorption characteristics of SLM fabricated Ti6Al4V triply periodic minimal surface cellular structures. Mech Mater 2022;166:104241.

[30] Ge J, Huang J, Lei Y, O'Reilly P, Ahmed M, Zhang C, Yan X, Yin S. Microstructural features and compressive properties of SLM Ti6Al4V lattice structures. Surf Coat Technol 2020;403:126419.
[31] Gibson LJ, Ashby MF. Cellular solids: structure and properties. 2nd ed.. Cambridge: Cambridge University; 1997.
[32] Shi G, Li L, Yu Z, Liu R, Sha P, Xu Z, Guo Y, Xi R, Liu J, Xin R, Chen L, Wang X, Zhang Z. The interaction effect of process parameters on the phase transformation behavior and tensile properties in additive manufacturing of Ni-rich NiTi alloy. J Manuf Process 2022;77:539–50. http://dx.doi.org/10.1016/j.jmapro.2022.03.027.
[33] Chu K, Sun Q. Reducing functional fatigue, transition stress and hysteresis of NiTi micropillars by one-step overstressed plastic deformation. Scr Mater 2021;201:113958. http://dx.doi.org/10.1016/j.scriptamat.2021.113958.
[34] Karamooz-Ravari MR, Taheri Andani M, Kadkhodaei M, Saedi S, Karaca H, Elahinia M. Modeling the cyclic shape memory and superelasticity of selective laser melting fabricated NiTi. Int J Mech Sci 2018;138–139:54–61. http://dx.doi.org/10.1016/j.ijmecsci.2018.01.034.
[35] Yang X, Yang Q, Shi Y, Yang L, Wu S, Yan C, Shi Y. Effect of volume fraction and unit cell size on manufacturability and compressive behaviors of Ni-Ti triply periodic minimal surface lattices. Addit Manuf 2022;54:102737. http://dx.doi.org/10.1016/j.addma.2022.102737.
[36] Zhang C, Jin J, He M, Yang L. Compressive mechanics and hyperelasticity of Ni-Ti lattice structures fabricated by selective laser melting. Crystals 2022;12(3):408. http://dx.doi.org/10.3390/cryst12030408.